J Mater Sci: Mater Electron (2021) 32:7073–7089

Influence of Sr/Nd partial replacement on fundamental properties of Bi-2223 superconducting system

M. Dogruer[1,*], C. Aksoy[2], G. Yildirim[3], O. Ozturk[4], and C. Terzioglu[5]

[1] Department of Medical Services and Techniques, Bolu Abant Izzet Baysal University, Bolu, Turkey
[2] Department of Electronics and Communication Engineering, Karadeniz Technical University, Trabzon, Turkey
[3] Department of Mechanical Engineering, Bolu Abant Izzet Baysal University, Bolu, Turkey
[4] Department of Physics, Kastamonu University, Kastamonu, Turkey
[5] Department of Physics, Bolu Abant Izzet Baysal University, Bolu, Turkey

Received: 14 December 2020
Accepted: 28 January 2021
Published online: 17 February 2021

ABSTRACT

This comprehensive work aims to examine the change in flux pinning mechanism, physical, mechanical, and structural characteristics of pure and Sr-site Nd-substituted $Bi_{1.8}Pb_{0.35}Sr_{1.9-y}Nd_yCa_{2.2}Cu_3O_x$ (Bi-2223) systems. The magnetoresistivity performances for all the samples are carried out by magnetotransport experiments in the existence of external magnetic field strength intervals 0–7 T. It is found that the increment of Nd/Sr substitution amount in bulk Bi-2223 system retrogrades the pinning capability of thermal flux motions for interlayer Josephson junction between the isolated grains. Similarly, the coupling probabilities of copper pairs and potential energy barriers are significantly diminished by increasing Nd impurity. This is in association with the enhancement of permanent structural problems in the crystal structure. Therefore, the excessive Nd inclusions improve the reattached linear/split pancake-like nature. In this regard, the best magnetic performance quantities are obtained for the pure sample. Besides, the SEM images show that the grain connectivity and surface morphology damage significantly with the Nd impurity. Additionally, the experimental microhardness findings conducted at various external loads (0.245–2.940 N) display that the Nd purity in the superconducting system degrades dramatically the key design mechanical features. Besides, we analyze the mechanical characteristic properties founded on the theoretical approaches with the proportional sample resistance, elastic/plastic deformation, and Hays–Kendall methods. The results obtained show that the Nd purity causes the indentation size effect behavior to decrease dramatically for all the samples. Furthermore, the findings of Hays–Kendall method are noticed to much more agree with the real hardness parameters. Thus, the Hays–Kendall model is the best methods to find the load-independent Vickers hardness values for the Sr-site Nd-substituted $Bi_{1.8}Pb_{0.35}Sr_{1.9-y}Nd_yCa_{2.2}Cu_3O_x$ (Bi-2223) systems. Moreover, in the dynamic microhardness measurements, the contact depth (h_c),

Address correspondence to E-mail: musadogruer@outlook.com

https://doi.org/10.1007/s10854-021-05417-4

elastic modulus (E_r), and load (P_{max}) of all the samples are experimentally recorded for the first time. The results reveal that the mechanical properties depend strongly on the load and Nd impurity level.

1 Introduction

The bismuth strontium calcium copper oxide (abbreviated as BSCCO) crystal structure was discovered in 1988 that displays superconductivity at 110 K and does not contain rare earth elements. Since then, the significant studies have been performed on BSCCO superconducting materials with the aim of improvement in the superconducting properties to meet the requirements of materials sciences, electro-optic, commercial, and heavy-industrial technology and advanced engineering application fields. Moreover, easy phase formation, cheap production method, no poisonous element content and relatively larger oxygen stability under even higher annealing temperature can be displayed as advantage for the BSCCO superconducting systems [1, 2]. At the same time, this superconducting material can be obtained as experimental in the atmospheric pressure because of their resistant to the humid atmosphere or water [3, 4]. The Bi-2223 superconducting phase (among the other phases of Bi-2212 and Bi-2201) is the most preferred material in the heavy-industrial technology and advanced engineering application fields owing to the highest critical transition temperature, current, and magnetic field-carrying capacities [5]. Nevertheless, some critic values such as large penetration depths, short coherence lengths, low charge carriers, and limited application temperature/magnetic field regions prevent the Bi- 2223 superconducting phase to be used in much more application fields [6, 7]. Furthermore, the existence of flux line movement towards the neighboring states as well as thermal fluxoid motions related to the 2D pancake vortices in the crystal structure does not allow the Bi-2223 superconductors to carry relatively higher critical currents in the application areas [8–12]. The researchers have obtained the mechanical durability and strength against to applied loads using the experimental measurement methods on the application-oriented material science [13–16]. Mechanical properties allow the superconductors use in energy-storage devices, magnetic coils, motors, power cables, transformers, refrigeration, magnets, generators, current-limiting devices, resonators, and levitated trains [17, 18]. In the current study, we struggle to form new flux pinning regions via the addition of Nd purities in the Bi-2223 matrix so that the restrictions mentioned are eliminated thoroughly.

Several authors have studied Nd addition on BSCCO superconducting materials [19–22]. The authors of Ref. [23] studied the Nd addition on Bi-2212 superconducting phase. According to this paper, the superconducting properties degrade with increasing the Nd impurity, presenting that the Nd addition is unfavorable for the formation of Bi-2212 materials. Bagiah et al. [24] displayed that the rare earth nanoparticle additions in the crystal system led to reduce the average crystallite size due to the enhanced grain orientations. According to the results observed, they proposed that both the nanoparticle size and magnetic properties belonging to the addition ions in the crystal lattice play an important role on the superconducting phase formations, change of lattice parameters, and electrical features of material. Aloysius et al. [25] obtained that the Nd impurity addition increased the flux pinning ability of bulk Bi-2223 ceramic materials. This study was carried out to find the effect of Nd_2O_3 nanoparticles on the electrical and structural properties of BiPbSrCaCuO superconducting materials. Ozkurt et al. [26] searched the influence of Nd/Pb partial substitution in the dilute concentrations for the $Bi_{1.7}Pb_{0.3-x}Nd_xSr_2Ca_3Cu_4O_{12+y}$ superconducting materials. Based on the results, a standard finding (decrement in the magnetization with the enhancement in the temperature) is obtained for the high-T_c materials.

In the current study, we report the effect of Sr-site Nd substitution on the structural, mechanical, magnetoresistivity performance, and flux pinning ability of the bulk $Bi_{1.8}Pb_{0.35}Sr_{1.9-y}Nd_yCa_{2.2}Cu_3O_x$ systems with x = 0, 0.01, 0.03, 0.05, 0.07, and 0.1 by the use of scanning electron microscope, Vickers microhardness, and magnetoresistivity measurements. Using the magnetoresistivity curves, we determine the upper critical field, irreversibility field, coherence length, and penetration depth values, which are useful parameters for the heavy-industrial

technology and advanced engineering application fields. Moreover, the experimental microhardness results are investigated by the theoretical models and discussed obviously. According to the SEM analysis, the dense and smooth view of surface morphology deteriorates with the increment in the Nd impurity level. Based on the results, it is found that electrical, physical, structural, mechanical, and flux pinning ability features of bulk $Bi_{1.8}Pb_{0.35}Sr_{1.9-y}Nd_yCa_{2.2}Cu_3O_x$ materials are varied by the Nd/Sr substitution mechanism.

2 Experimental procedures for the preparation of Bi-2223 materials

In the present study, the pure and partial substitution of different aliovalent Nd-sites (Nd^{3+}) at Sr-sites (Sr^{2+}) in the $Bi_{1.8}Pb_{0.35}Sr_{1.9-y}Nd_yCa_{2.2}Cu_3O_x$ cuprate-layered perovskite superconducting materials ($0 \leq x \leq 0.1$) are performed by the solid-state reaction using high-purity chemicals such as Bi_2O_3, PbO, $SrCO_3$, $CaCO_3$, CuO, and Nd_2O_3 (Alfa Aesar Co., Ltd. 99.9% purity). The compounds weighed in grinding stoichiometric amount are exposed to the mixing process for the period of 24 h in the grinder. Then, the powder is calcined twice, first at 750 °C for 12 h and second at 800 °C for 24 h in air with a heating/cooling rate of 5 °C/min. Between two calcinations and afterwards, the powder is mixed in the grinding machine for 2 h. After the calcination, the powder is pressed into rectangular bars with dimensions of 10 x 4 x 2 mm^3 at 200 MPa. The sintering is performed in three main heating stages at 835 °C for 24 h; 840 °C for 48 h and again the temperature of 840 °C for 48 h. After the first stage sintering the bulk sample is pulverized by applying 100 MPa between two steel plates and then mixed in the grinding machine for 2 h. Then, the powder is re-annealed at 840 °C for 48 h in the air at the same cooling and heating rates and again pelletized using the same force. As for the last sintering process, the bulk samples are reground for 5 min in a mortar and pelletized using a rectangular bar of 10 × 4 × 2 mm^3 under a force of 200 MPa at the room temperature. The final heat process is performed at 840 °C for 48 h in the atmospheric air to give the Bi-2223 superconducting phase to the materials.

3 Experimental characterization of every superconducting materials

The dc resistivity measurements are performed on the sample using the four-probe method. To minimize the contact resistance, both current and voltage contacts are covered with silver paint. The change of the resistivity as a function of the temperature is measured by running 5 mA dc current through the sample in the cryostat using a Keithley 2182A nanovoltmeter and a Keithley 220 programmable current source. The experimental signals are collected with programmable nano-voltmeter and current source with an accuracy of about ± 0.1 K using Labview software. The measurement results are automatically gathered by Labview software. Further, the microstructural characterization is performed on a SEM JEOL 6390-LV scanning electronic microscope (SEM) operated at 20 kV with a resolution power of 3 nm. At 300 K, the experimental examinations are performed by a SHIMADZU HVM-2 model digital tester. The test load is applied to the specimen surface from 0.245 to 2.940 N for 10 s. Average of microhardness values measured from different parts of the sample surface gives optimum microhardness values. The accuracy for the impression diagonals is noted to be about ± 0.1 μm and the distance between two indentation diagonals is determined by a microscope. A Vickers indenter is used in a dynamic microhardness tester (UMT—Bruker SYS2). For examination of the material performance at different depths, the load is variated at systematic intervals as 1, 2, 3, 4, and 5 N, where time is at 10 s every load. In the dynamic microhardness measurements, the contact depth (h_c), elastic modulus (E_r), and the load (P_{max}) are recorded by a computer. Then, these raw data are used to obtain the load–depth plots.

The superconductor samples produced with different Nd stoichiometry such as 0, 0.01, 0.03, 0.05, 0.07, and 0.1 will hereafter be denoted as Nd0, Nd1, Nd2, Nd3, Nd4, and Nd5, respectively.

4 Results and discussion

4.1 Magnetoresistivity measurements

We examine the effect of Nd inclusions on the magnetoresistivity properties of Bi-2223 materials by the way of temperature-dependent electrical resistivity

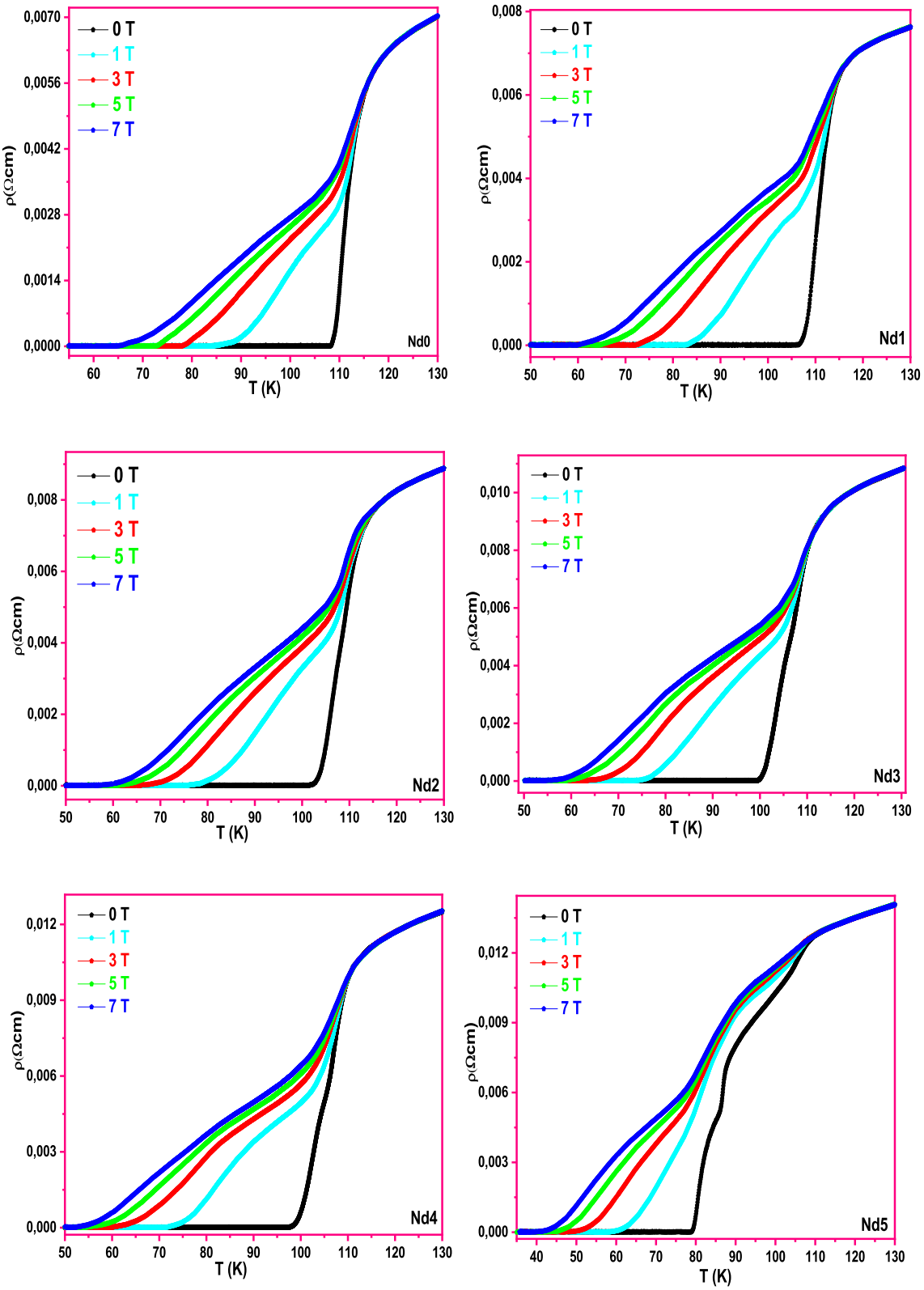

Fig. 1 Temperature dependence of resistivity for all samples under different applied magnetic fields

measurement exerted at magnetic fields (0 T ≤ μ_0-H ≤ 7 T). One can see the experimental magnetoresistivity curves for all samples in Fig. 1. Both the presence of Nd purity and applied magnetic field are influenced the magnetoresistivity characteristics. The critical temperature (T_c^{offset}) determined from the superconducting phase fractions containing various phases in superconducting system is in association with inter-granular component properties. Moreover, at the temperature below the T_c^{offset} parameter, the bulk Bi-2223 ceramic displays completely the superconducting features. The critical temperature (T_c^{onset}), where the electron–phonon link determines the superconductivity, means transition of the isolated grains into the superconducting state [27]. Additionally, the T_c^{onset} is in correspondence with the metastability and trap energy of itinerant charge carrier concentrations in the in-plane Cu–O_2 sheets [28]. On this basis, at the temperatures higher than the T_c^{onset} parameter, the superconductivity quickly disappears owing to the destruction of cooper-pair couplings and starting of thermal fluctuations of 2D vortices. One can see all the T_c^{offset} and T_c^{onset} parameters deduced from the magnetoresistivity curves in Table 1. According to the table, the decreasing in the T_c^{onset} values with the Nd impurities causes the general structural problems: distortions, defects, grain misorientations, lattice strains, disorders, and coupling problems between the grains in the active Cu–O_2 layers [29]. At the Fermi energy level, the T_c^{onset} and T_c^{offset} values demonstrated that the hole-filling mechanism begins for the dynamic and active electronic densities of state [30, 31]. All in all, the Nd0 superconducting compound possesses the highest T_c^{onset} (116.5 K) and T_c^{offset} (108.4 K) values at 0 T, respectively. From the table, the excess Nd impurity level damages the magnetic field-carrying capacity owing to the deterioration in the elastic moduli for the vortex lattice and especially Josephson link length [32]. Additionally, the T_c^{offset} values of the pure sample obtain to reduce from 108.4 to 65.3 K with the increase in the magnetic field up to the 7 T. Hence, with the increment of Nd purities and applied magnetic field, the nucleation centers serving as the flux pinning areas are found to decrease dramatically and thus, the pinning capability of 2D pancake vortices more and more weakens due to the decrement in the connection between the adjacent layers in the crystal system. According to pair-breaking theory, the decrease in the T_c^{offset} parameters depending on the applied magnetic field is attributed to the connection between the quantum spin number of magnetic impurity and conduction electron spin number of super-electrons [33]. It is another important result determined from Fig. 1 that the Nd4 and especially Nd5 compounds exhibit a pseudo-transition in the temperature-dependent resistivity curves due to the presence of impurity phases, namely, the Bi-2212 and Nd-related impurity phases. In other words, the materials mentioned above present the double transitions founded on the low Bi-2212 superconducting phase. Besides, the induced permanent local structural problems in the crystal lattice with the excess Nd impurity result in the possible double transitions for the Bi-2223 superconducting system.

Table 1 T_c^{onset} and T_c^{offset} values of the samples at various applied magnetic field

Samples	T_c^{onset} (K)	T_c^{offset} (K)				
		0 T	1 T	3 T	5 T	7 T
Nd0	116.5	108.4	85.2	77.9	72.9	65.3
Nd1	115.8	106.5	82.9	72.4	65.5	60.7
Nd2	115.1	102.4	77.9	67.1	61.3	57.4
Nd3	110.5	99.4	74.3	63.6	59.3	55.9
Nd4	109.9	97.6	71.6	59.8	54.3	52.2
Nd5	108.7	78.8	58.4	48.8	45.1	40.2

4.2 Flux pinning energy

Flux pinning (activation) energy values of pure and Sr/Nd replacement in Bi-2223 superconducting materials are computed by Arrhenius law

$$\rho = \rho_0 exp\left(\frac{U_0}{k_B T}\right), \quad (1)$$

where ρ_0 is a field-independent exponential parameter, U_0 is the activation (pinning) energy, and k_B is Boltzmann's constant [34]. We calculate the activation energy values of pure and Nd-substituted Sr-site in Bi-2223 crystal using the slopes deduced from the broadening tails as shown in Fig. 2. Activation energy (U_0) values calculated are presented in Table 2. It is seen that the U_0 values tend to reduce regularly with the enhancement of both Nd impurities and magnetic field. This is attributed the fact that the pinning ability for 2D pancake vortices is

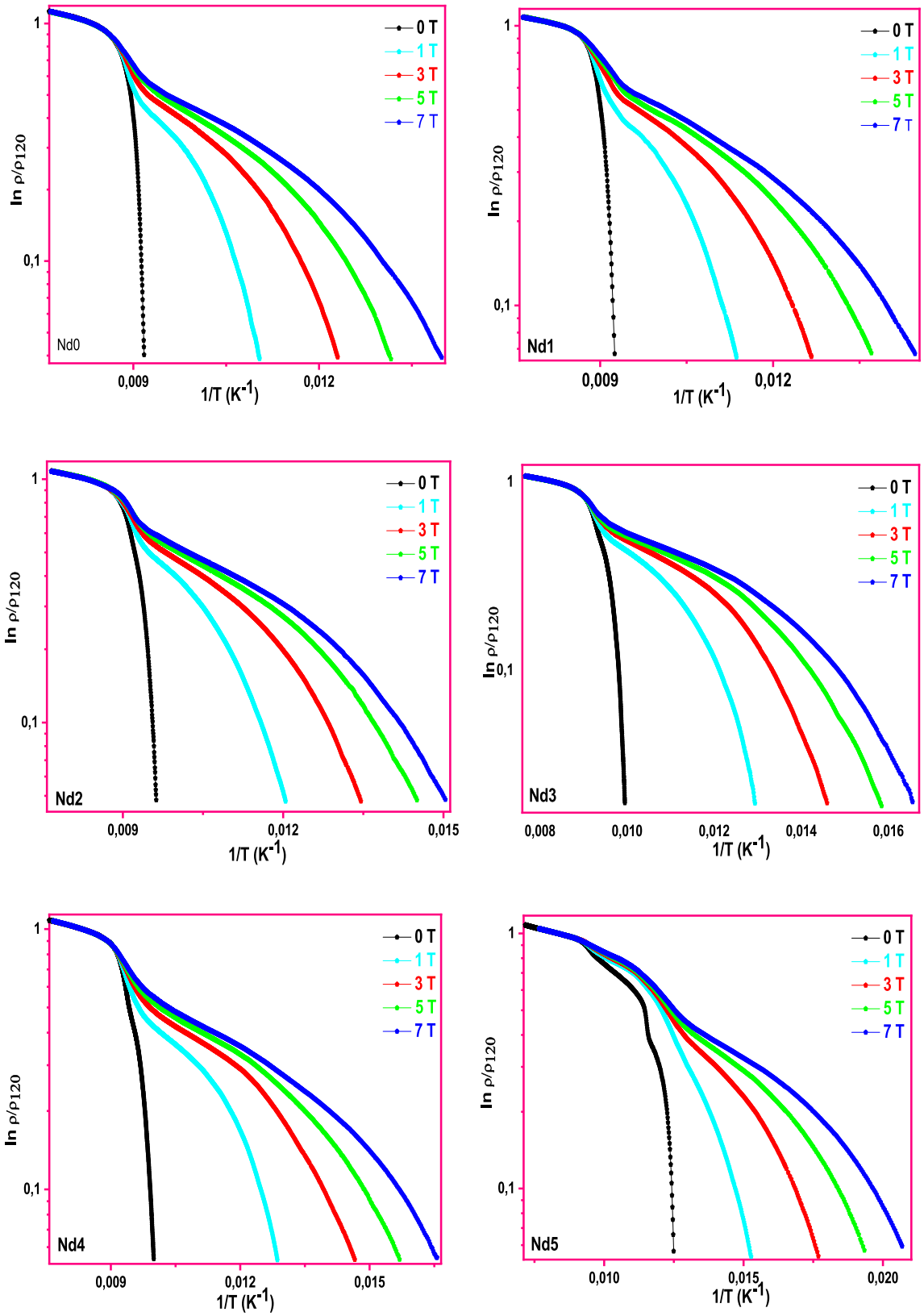

Fig. 2 Arrhenius plots of the normalized resistivity of every samples under the various magnetic fields

Table 2 Pinning (activation) energy values of the pure and Sr-site Nd-substituted Bi-2223 superconductors

Samples	Pinning (activation) energies (K)				
	0 T	1 T	3 T	5 T	7 T
Nd0	2351.8	1186.8	792.2	587.7	440.3
Nd1	1905.2	950.9	582.3	445.1	420.9
Nd2	1232.2	710.9	493.2	418.4	383.6
Nd3	954.3	612.1	448.5	385.9	347.1
Nd4	901.3	557.3	395.6	327.4	316.8
Nd5	674.7	216.6	171.5	148.5	122.1

thermally disrupted by the increase of magnetic fields. At the zero magnetic field, the pinning energy value of pure sample is obtained as 2351.8 K, while Nd5 sample is computed to be about 674.7 K (Table 2). At 7 T magnetic field, the highest flux pinning energy parameter is attained to be about 440.3 K for the bulk Nd0 material, while the lowest value of about 122.1 K is found for the bulk Nd5 compound, presenting clearly the diminish in both the energy barriers and the spacing between the pinning areas [35].

4.3 Irreversibility and upper critical field

The irreversibility field ($\mu_0 H_{irr}$) and upper critical field ($\mu_0 H_{c2}$) were deduced from the resistivity versus the applied magnetic field curves. Temperature-dependent magnetoresistivity values over the external field applied are provided with the following relations [36, 37].

$$\rho(\mu_0 H_{\mathrm{irr}}, T) = 0.1\rho_n \mu_0 H_{\mathrm{irr}}(T), \quad (2)$$

$$\rho(\mu_0 H_{c2}, T) = 0.9\rho_n \mu_0 H_{c2}(T), \quad (3)$$

ρ_n presents normal state resistivity for the $Bi_{1.8}Pb_{0.35}Sr_{1.9-y}Nd_yCa_{2.2}Cu_3O_x$ superconductors at the temperature of 120 K. One can encounter the differentiation of $\mu_0 H_{irr}$ and $\mu_0 H_{c2}$ parameters against temperature for every sample in Fig. 3a, b. The theoretical results obtained are numerically summarized in Table 3 in detail. The $\mu_0 H_{irr}$ and $\mu_0 H_{c2}$ values reduce with increment of Nd additives due to the decrease in the pinning capability (associated with the pinning force) [38]. According to table, the highest parameters ascribe to unsubstituted Bi-2223 superconducting ceramic material whereas the bulk Nd5 compound has the deepest $\mu_0 H_{irr}$ and $\mu_0 H_{c2}$

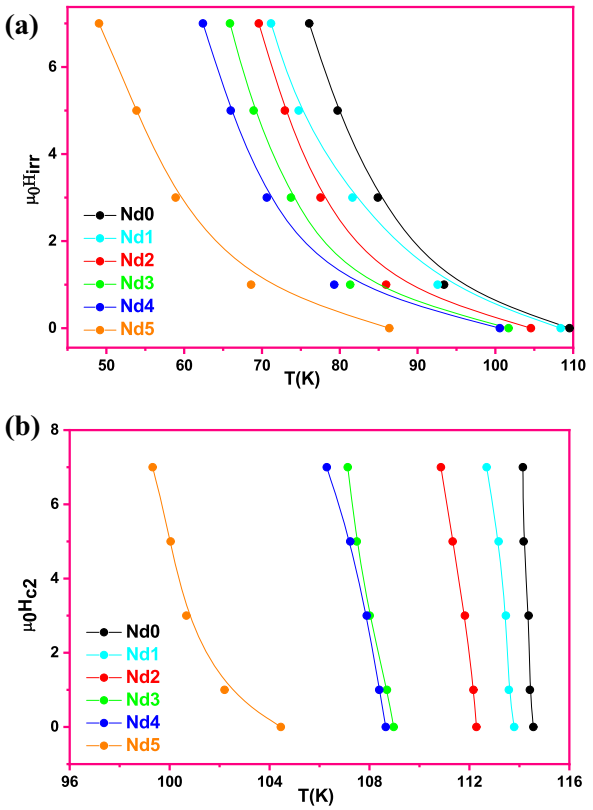

Fig. 3 **a** The temperature dependences of the irreversibility field for all samples. **b** The temperature dependences of the upper critical field for all samples

Table 3 Irreversibility field, upper critical field, coherence length and penetration depth values of the samples

Samples	$\mu_0 H_{\mathrm{irr}}$ (0) (T)	$\mu_0 H_{c2}$ (0) (T)	ξ_0 (Å)	λ_0 (Å)
Nd0	20.73	1799.00	39.9	4.28
Nd1	18.44	747.67	42.3	6.64
Nd2	18.29	540.02	42.4	7.81
Nd3	17.03	394.64	44.0	9.14
Nd4	15.81	324.20	45.6	10.08
Nd5	14.52	135.58	47.6	15.59

values, confirming that the excess Nd purity harms the flux pinning mechanism. According to Fig. 3b, there are large gaps for the temperature dependencies of $\mu_0 H_{c2}$ between the Nd2 and Nd3 samples and similarly between Nd4 and Nd5 samples. This fact is noteworthy that the increase of Nd inclusion in the Bi-2223 system deteriorates considerably the vortex lattice elasticity and lattice period due to the reduction of vortex pinning capability.

4.4 Penetration depth and coherence length and

We deal with the variation in the quantum mechanical quantities including the penetration depth (λ) and coherence length (ξ) with the Sr/Nd substitution using the relationship between upper critical magnetic field and irreversibility critical magnetic field parameters. In more detail, ξ (0) and λ (0) parameters at 0 K are defined as,

$$\lambda(T) = \left[\frac{\varphi_0}{2\pi\mu_0 H_{c2}(T)}\right]^{\frac{1}{2}}, \tag{4}$$

$$\xi(T) = \left[\frac{\varphi_0}{2\pi\mu_0 H_{\mathrm{irr}}(T)}\right]^{\frac{1}{2}}, \tag{5}$$

where φ_0 is equal to 2.07×10^{-15} Tm^2. All the computations are numerically inserted in Table 3. It is visible from the table that every ξ (0) and λ (0) value tends to enhance systematically depending on the Nd inclusions in the Bi-2223 crystal structure. Based on the results obtained, the Nd impurities result in the reduction of energy barrier level and accordingly 2D pancake vortex formation accelerates immediately [39].

4.5 SEM analyses

Figure 4 shows the surface micrographs of pure and Sr-site Nd-substituted Bi-2223 materials. It is seen that all the compounds studied in the current work exhibit the similar microstructures with the platelet-like grain size growth. On this basis, it is to be mentioned here that the presence of Nd impurities in the hole-induced Bi-2223 system seldom damages the main crystal matrix. However, some negative changes on the surfaces are obtained. In more detail, the random alignment distributions of superconducting grains tend to enhance monotonously with the enhancement in the partial Sr/Nd substitution level up to the maximum level. Likewise, the voids are noted to increase dramatically depending on the Nd impurity level. In this regard, the undoped sample with clear and flaky layers of large platelet-like structure is observed to possess much smoother and denser surface, while the Nd5 sample with the worst crystal structure has more voids. Besides, the figure shows that after the critical replacement level of $x = 0.07$, there seems melting formations in some regions of main texture as a result of not only the rapid increment of inhomogeneity especially and liquid phase formations (founded on the impurity phases) but also the decrement in the crystallinity quality of material. We give some detail for the voids (provided in yellow color) and melting formations (depicted in red color) for the Nd5 sample in detail. Furthermore, the layered grain growth of pure sample is obtained to be better compared to those of other ones. Consequently, the surface morphology and grain connectivity (the enhanced grain boundary coupling strength) are obtained to damage significantly with the enhancement of Nd purity level in the crystal system.

4.6 Examination of Vickers hardness experimental results by static microindentation technique

We demonstrate the effect of Nd purities on the mechanical characteristic of bulk Bi-2223 systems by the differentiation in impression sizes (d) over the test loads (F). Namely,

$$H_V = 1854.4\left(\frac{F}{d^2}\right), \tag{6}$$

where H_v is the Vickers hardness parameters. The experimental obtained impression size and calculated H_v values are gathered in Table 4. The H_v values depend on the Nd impurities and indentation loads. The highest H_v value is obtained as 0.984 GPa for Nd0 material. The reduce in the H_v values with the increment of Nd additives leads to augment in the general structural problems in the in-plane Cu–O_2 sheets and grain boundary weak-links. Therefore, the increase of Nd nanoparticles enables the propagation of voids and cracks in the superconducting system reach to the critical velocity easily. Figure 5 demonstrates the relation between the Vickers microhardness parameters and applied loads for every sample. It is obvious from the figure that all samples show the indentation size effect (*ISE*) [40]. That is to say, the Vickers hardness parameters of superconducting compounds decrease dramatically as the applied load increases [41]. Every sample decreases non-linearly with the increase in the applied load up to 2 N after which a small change is found because of the influence of the plateau (saturation) region, providing that at the small applied loads, the surface effect becomes more dominant.

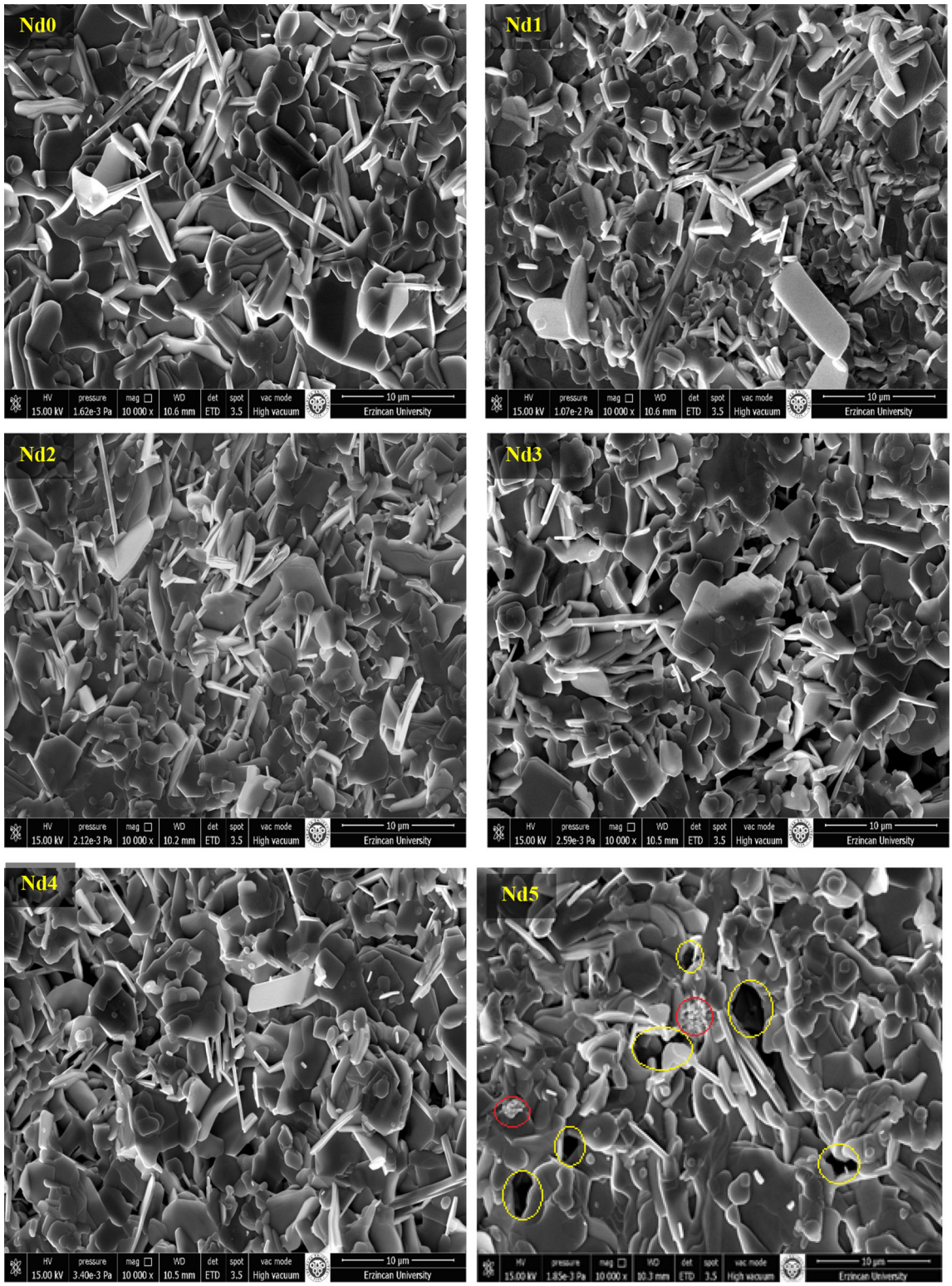

Fig. 4 SEM micrographs belonging to every samples

Table 4 Variation of load dependent microhardness parameters as a function of applied indentation test loads for the pure and Sr/Nd-substituted bulk Bi-2223 compounds

Samples	d (μm)	F (N)	H_v (GPa)
Nd0	21.48	0.245	0.984
	31.39	0.490	0.922
	46.06	0.980	0.856
	66.86	1.960	0.813
	83.34	2.940	0.784
Nd1	21.93	0.245	0.944
	32.53	0.490	0.858
	47.54	0.980	0.804
	69.42	1.960	0.754
	86.41	2.940	0.730
Nd2	22.22	0.245	0.920
	34.84	0.490	0.748
	52.11	0.980	0.669
	75.64	1.960	0.635
	93.64	2.940	0.621
Nd3	23.85	0.245	0.798
	36.36	0.490	0.687
	54.62	0.980	0.609
	81.13	1.960	0.552
	100.87	2.940	0.535
Nd4	25.61	0.245	0.692
	39.53	0.490	0.581
	59.71	0.980	0.509
	88.83	1.960	0.460
	110.6	2.940	0.445
Nd5	26.76	0.245	0.634
	42.35	0.490	0.506
	63.88	0.980	0.445
	94.69	1.960	0.405
	117.36	2.940	0.395

4.6.1 *Analysis of load-independent hardness by static microindentation technique according to proportional sample resistance model*

The indentation test load (F) and the diagonal length (d) are found by the following formula [42]:

$$\frac{F}{d} = \alpha + \beta d. \tag{7}$$

One can see numerically every surface energy (α) value and hardness constant (β) calculated for all the materials in Table 5 in detail. From the table, the proportional sample resistance (PSR) model shows the ISE nature because of the values of α are positive. The linear curves for the applied load F/d versus diagonal length d are shown in Fig. 6. The H_{PSR} can be obtained from hardness constants:

$$H_{PSR} = 1854.4\beta. \tag{8}$$

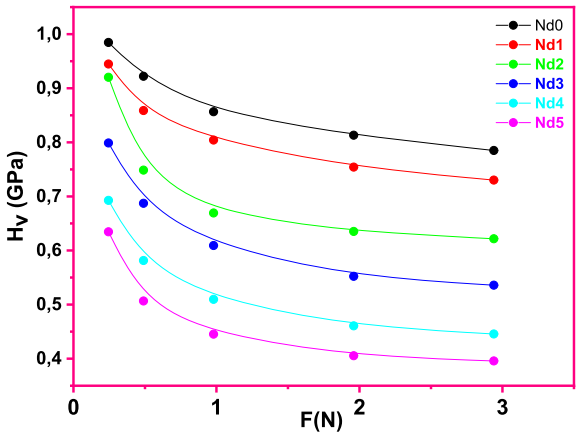

Fig. 5 Variation of Vickers microhardness parameters of the pure and Sr/Nd-substituted Bi-2223 ceramic materials against applied static test loads

It is a significant point found from the Table 6; the H_{PSR} values computed by PSR model are smaller than the H_v values and also the H_{EPD} values decrease with increasing of the Nd impurity. Furthermore, the obtained H_v values are far from the H_{PSR} values, presenting that the PSR model may be insufficient to define the real hardness values of superconducting materials.

4.6.2 *Explanation of true Vickers microhardness parameters with elastic/plastic deformation model*

The dependence of indentation size on the applied load is calculated by following relation [43]:

$$F = A_{EPD}(d_e + d_p)^2, \tag{9}$$

where A_{EPD} is a constant, and elastic deformation d_e is associated with plastic deformation d_p. Figure 7 reveals the applied load dependence of the indentation diagonals studied using $F^{1/2}$ versus d_p plots. The A_{EPD} and d_e values deduced from Fig. 7 are represented in Table 5. Based on these results from Table 5, every sample possesses the positive d_e value, confirming that the elastic and plastic deformation is found together in the material. The last descriptor shows that all the materials studied exhibit the ISE performance. Moreover, the load-independent hardness parameters are calculated by the formula:

Table 5 Experimental results and theoretical calculation data related on PSR model, EPD Model and HK approaches

Samples	HK model		EPD model		PSR model	
	W_{HK} (N)	$A_{HK} \times 10^{-4}$(N/μm^2)	d_e (μm)	A_{EPD} (N/μm^2)	$\alpha \times 10^{-3}$ (N/μm)	$\beta \times 10^{-4}$(N/μm^2)
Nd0	0.0797	4.1486	0.07833	0.0197	3.3823	3.8523
Nd1	0.0846	3.8494	0.08469	0.0189	3.5444	3.5444
Nd2	0.0922	3.2537	0.10677	0.0171	4.2364	2.8739
Nd3	0.1170	2.7876	0.12338	0.0157	4.5561	2.4329
Nd4	0.1241	2.3138	0.13207	0.0143	4.4859	1.9919
Nd5	0.1185	2.0533	0.13205	0.0134	4.2486	1.7556

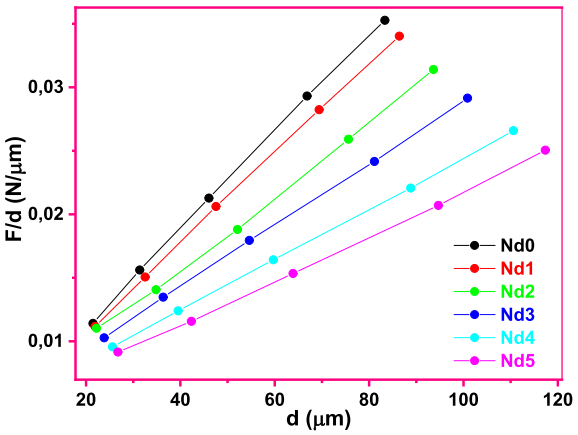

Fig. 6 Variation of applied test load F/d versus indentation diagonal length d for every samples

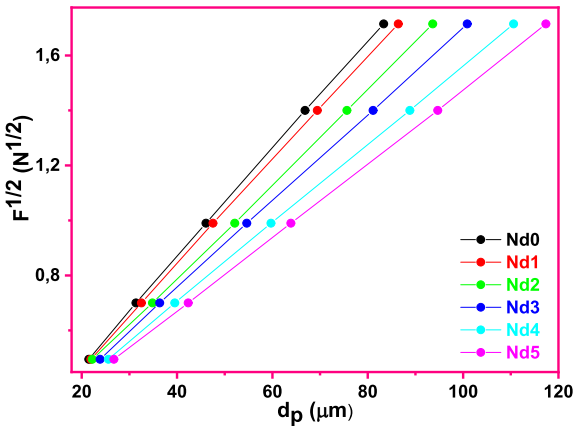

Fig. 7 Linear curves between static load $F^{1/2}$ and diagonal length d_p for all samples

Table 6 The results of calculated values of H_V, H_{PSR}, H_{EPD} and H_{HK} Model

Samples	H_{PSR} (GPa)	H_{EPD} (GPa)	H_{HK} (GPa)	H_V (GPa)
Nd0	0.714	0.719	0.769	0.784–0.813
Nd1	0.657	0.663	0.713	0.730–0.754
Nd2	0.532	0.543	0.603	0.621–0.635
Nd3	0.451	0.461	0.516	0.535–0.552
Nd4	0.369	0.379	0.429	0.445–0.460
Nd5	0.325	0.335	0.380	0.395–0.405

$$H_{EPD} = 1854.4A_{EPD} \tag{10}$$

From the Table 6, the H_{EPD} values reduce with the increment of the Nd content. The load-independent hardness value (H_{EPD}) computed by elastic/plastic deformation model is far from the real hardness value for Bi-2223 samples. Consequently, the elastic/plastic deformation model may also be insufficient to define the ISE nature.

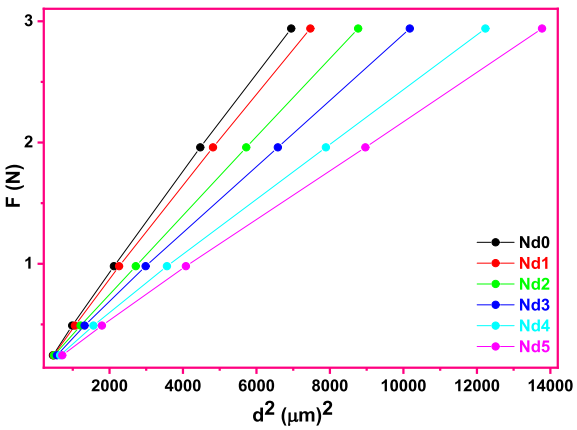

Fig. 8 Linear plots of indentation test load F over indentation impression length d^2 of the pure and Sr-site Nd-substituted ceramics

4.6.3 *Investigation of real microhardness parameters with Hays–Kendall approach*

The indenter enters deeply into the superconducting samples in the presence of test load (called as W_{HK})

applied. Hence, the indentation distance can be extracted from effective load of $F_{eff} = F - W_{HK}$ using the formula [44]:

$$F = W_{HK} + A_{HK}d^2, \tag{11}$$

where A_{HK} is hardness constant. Based on the HK method, the true Vickers hardness (H_{HK}) is computed by:

$$H_{HK} = 1854.4A_{HK}. \tag{12}$$

Figure 8 illustrates the plots of (F) versus (d^2) according to Hays–Kendall methods. The slope of the line found every sample is equal to the constant A_{HK} and intersection of W_{HK}, which characterizes the resistive pressure of the samples. The found best-fit parameters of A_{HK} and W_{HK} are tabulated in Table 5. The W_{HK} values are obtained positively for every sample, which means that the applied load is adequate to produce elastic and plastic deformation. Based on results obtained from Table 6, the values of H_{HK} decrease with the increment of the Nd addition. The H_{HK} value is closer to the saturation value compared with the results of the other models. Consequently, the HK approach is the most suitable method to examine the mechanical characteristic of the Bi-2223 materials.

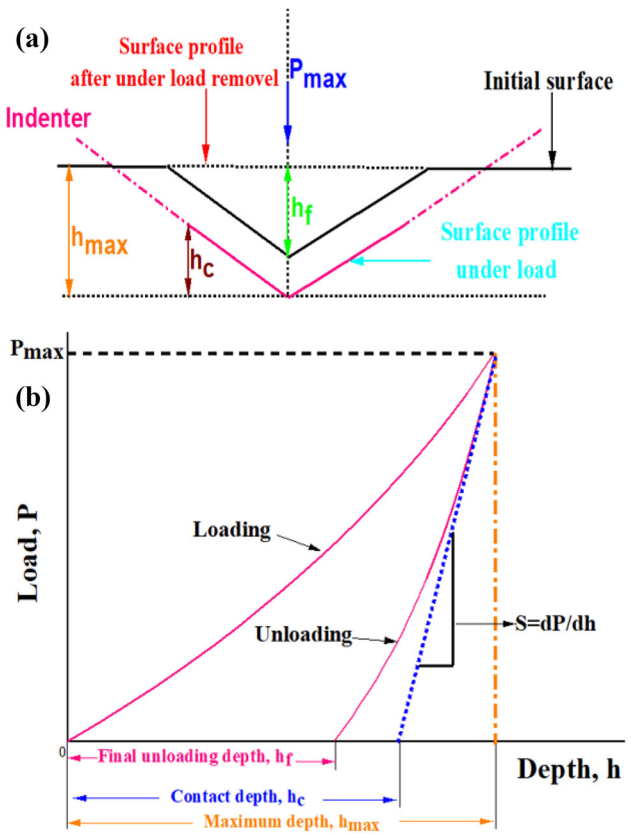

Fig. 9 **a** Cross-section view of indentation, **b** example load/unload–depth curve

4.7 Microhardness characteristics studied by dynamic microindentation technique

4.7.1 *Theoretical background*

Typical load-indentation depth curve produced during depth indentation experiment, demonstrating the key parameters required for investigation is shown in Fig. 9. Test material during indentation loading is exposed to both elastic and plastic deformation. The key values required to define the hardness are the contact area (A_c), initial unloading contact stiffness (S) and peak load (P_{max}). Further, the microhardness (H) is described by following relation [45]:

$$H = \frac{P_{\max}}{A_c} = \frac{P_{\max}}{24.5h_c^2} \tag{13}$$

where h_c is the contact depth, $Ac = \pi h_c^2 tan^2\alpha = 24.5h_c^2$ is the area of the indentation impression and therefore the half angle for a corresponding conical indenter is 70.3°. The various methods for extracting the contact depth (h_c) are suggested by Oliver and Pharr [46].

$$P = a(h - h_f)^m, \tag{14}$$

where P presents the indentation load, h displays the penetration depth, h_f is the final unloading depth and α and m are fitting parameters. From the unloading curve, stiffness and contact depth are deduced by Eq. 14 at the maximum depth of penetration, ($h = h_{max}$). Then, the stiffness value is demonstrated by following equation [47]

$$S = \left|\frac{dP}{dh}\right| = \frac{2}{\sqrt{\pi}} E_r \sqrt{A_c}, \tag{15}$$

where E_r is the reduced elastic modulus. In this work, the Oliver and Pharr method are used to measure the contact depth (h_c), reduced modulus (E_r) and hardness (H).

4.7.2 *Investigating of load–depth curves*

The load versus depth graphs displayed in Fig. 10 present the applied load as a function of the depth of

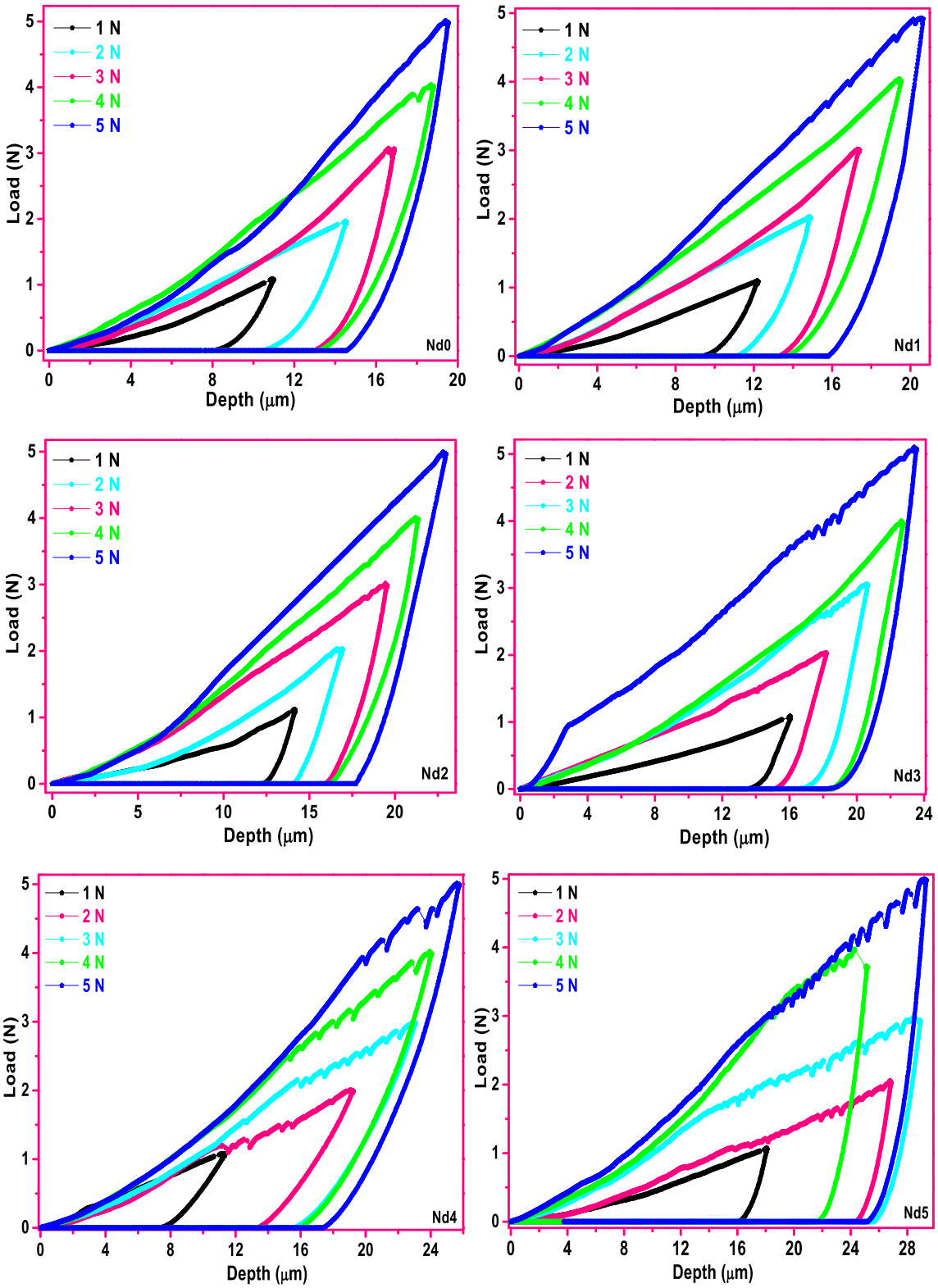

Fig. 10 Loading/unloading–depth curve for every samples

Table 7 Results of dynamic microindentation analysis for each sample

Sample	P_{max} (N)	h_c (μm)	H (GPa)	E_r (GPa)	S (N/μm)
Nd0	1.0	10.071	0.412	15.038	0.845
	2.0	12.961	0.484	17.163	1.242
	3.0	15.299	0.523	19.883	1.699
	4.0	16.989	0.564	22.737	2.157
	5.0	18.013	0.622	24.768	2.491
Nd1	1.0	11.062	0.333	14.055	0.868
	2.0	13.273	0.463	16.347	1.211
	3.0	15.562	0.505	19.122	1.662
	4.0	17.704	0.520	21.696	2.145
	5.0	18.534	0.594	22.447	2.323
Nd2	1.0	13.170	0.235	13.391	0.985
	2.0	15.380	0.345	14.762	1.268
	3.0	18.145	0.367	16.020	1.623
	4.0	19.638	0.419	16.101	1.766
	5.0	20.969	0.464	21.380	2.504
Nd3	1.0	15.133	0.185	12.673	1.071
	2.0	16.657	0.294	13.908	1.293
	3.0	18.792	0.345	15.344	1.610
	4.0	20.554	0.386	15.790	1.812
	5.0	22.007	0.424	20.646	2.537
Nd4	1.0	9.2973	0.491	7.507	0.389
	2.0	16.262	0.306	5.527	0.502
	3.0	19.678	0.312	6.002	0.659
	4.0	20.725	0.378	7.825	0.905
	5.0	22.657	0.393	9.619	1.217
Nd5	1.0	17.381	0.139	11.358	1.102
	2.0	25.835	0.122	10.782	1.555
	3.0	27.666	0.158	11.551	1.784
	4.0	23.773	0.286	16.500	2.190
	5.0	28.065	0.256	19.141	3.000

the indenter in point of the first position of surface. It is obvious from the Table 7 that the contact depth of Nd0 sample for each applied peak load is found to be lower than that of Nd1, Nd2, Nd3 and Nd5 samples (except for the Nd4 sample), which implies the higher hardness for Nd0 samples. Further the minimum h_c values obtained for the Nd4 sample at 1.0 N applied load confirm to exhibit the greatest hardness values. Additionally, the experimental hardness values obtained increase with the applied load for the Nd0, Nd1, Nd2, Nd3 and Nd4 samples (except Nd4 sample at 1.0 N applied load). At the same time, the obtained H value for the Nd5 sample changes randomly, providing that the Nd5 sample has more voids in the SEM examination. In addition, the E_r experimental values found are described in Table 7. From the table, E_r parameters increment with increasing the peak load except for Nd5 at 2.0 N applied load. The Nd4 compound displays the smallest E_r values. This is associated with the fact that the variation of $h_{max} - h_c$ values is recorded to be the highest among every sample. The calculated values of stiffness from Eq. 15 are summarized in Table 7. The stiffness values increase with the increase in the applied load for every sample. The Nd4 sample has the minimum S values because of the fact that the variations of $h_{max} - h_c$ values are noted to be greater than those of other samples. Another significant parameter of mechanical characteristics is pop-in and pop-out feature. There is no obtained pop-out from the unloading part in Fig. 10. Furthermore, the pop-in feature from the loading part is not found for every sample at 1.0 applied load. However, with increasing the applied load (after 1.0 N applied load), the pop-in is observed for all the superconducting compounds studied in the current work. According to the approaches defined in the literature, the pop-in can be caused by the voids in the microstructure or defects such as formation of cracks and dislocations during the indentation [48–50].

5 Conclusions

Based on the results of magnetoresistivity, scanning electron microscope and microhardness examination of $Bi_{1.8}Pb_{0.35}Sr_{1.9-y}Nd_yCa_{2.2}Cu_3O_x$ superconductors, the following conclusions can be drawn:

- The T_c^{onset} and T_c^{offset} values decrease with increasing Nd impurities and applied magnetic field, and also the maximum values are obtained for the Nd0 sample of 116.5 K and 108.4 K at 0 T, respectively.
- The obtained minimum T_c^{offset} value for the Nd5 sample is 40.2 K at 7 T.
- Both the $\mu_0 H_{irr}$ (0) (T) and $\mu_0 H_{c2}$ (0) (T) values are found to reduce with the increase Nd inclusions as a consequence of the deterioration of the flux pinning.
- The coherence lengths increase from 39.9 to 47.6 Å; likewise, the penetration depths increment from 4.28 to 15.59 Å with the increase Nd purity, providing that the physical quantities of the Bi-2223 samples degrade frequently.

- The highest U_0 value is found for the Nd0 sample as compared with the other ones because of the strong pinning effect of the vortices and increase of the vortex pining force, showing that the Nd0 sample can carry maximum current in the existence of magnetic field.
- The SEM pictures demonstrate that the dense surface with a fine connectivity between the grain damages with the Nd inclusions, causing the retrograde of the surface morphology.
- The results of the static microindentation H_v values show that every sample exhibit indentation size effect (*ISE*) behavior.
- The H_{PSR} values are found to be lower than the true microhardness in the plateau regions. Though studying the difference of mechanical properties with the addition, the PSR model is unsuitable approach to evaluate the load-independent microhardness values.
- EPD model is unsuitable for the determination of the true microhardness value.
- As can be seen that the H_{HK} values are obtained to be closer to the load-independent hardness values. Consequently, the HK model is appropriate theoretical approach to inspect the mechanical characteristics of superconducting materials.
- At the dynamic microindentation hardness, while the H values increase with the applied load magnitudes (except for the Nd4 sample at 1.0 N applied load), for the Nd5 sample, the H values are observed to vary arbitrarily.
- The experimental obtained E_r values increase with peak load except for Nd5 at 2.0 N. Moreover, the minimum E_r values are found for Nd4 sample, providing that the $h_{max} - h_c$ values are greatest than other samples
- The stiffness values enhance with the increment of the applied load for the all samples.
- The pop-out is not obtained for every sample, while the pop-in is found for all the samples except at 1.0 applied load

Acknowledgements

This study is supported by Bolu Abant Izzet Baysal University Scientific Research Project Coordination Unit (Project No: 2016.03.02.1024).

References

1. W.E. Pickett, Electronic-structure of the high-temperature oxide superconductors. Rev. Mod. Phys. **61**, 433–512 (1989)
2. A. Biju, R.P. Aloysius, U. Syamaprasad, Enhanced critical current density in Gd added (Bi, Pb)-2212 bulk superconductor. Supercond. Sci. Technol. **18**, 1454–1459 (2005)
3. M.E. Takayama, High-pressure synthesis of homologous series of high critical temperature (T_c) superconductors. Chem. Mater. **10**, 2686–2698 (1998)
4. H. Yamauchi, M. Karppinen, Application of high-pressure techniques: stabilization and oxidation-state control of novel superconductive and related multi-layered copper oxides. Supercond. Sci. Techol **13**, R33–R52 (2000)
5. B.R. Lehndorff, *High-Tc Superconductors for Magnet and Energy Technology Superconductors for Magnet and Energy Technology* (Springer, New York, 2001).
6. K. Koyama, S. Kanno, S. Noguchi, Electrical, magnetic and superconducting properties of the quenched $Bi_2Sr_2Ca_{1-x}Nd_xCu_2O_{8+y}$ system. Jpn. J. Appl. Phys. **29**, L53–L56 (1990)
7. H. Miao, M. Meinesz, B. Czabai, J. Parrell, S. Hong, Microstructure and $J(_c)$ improvements in multifilamentary Bi-2212/Ag wires for high field magnet applications. AIP. Conf. Proc. **986**, 423–430 (2008)
8. L. Zhou, P. Zhang, P. Ji, K. Wang, X. Wu, The properties of YBCO superconductors prepared by a new approach-the powder melting process. Supercond. Sci. Technol. **3**, 490–492 (1990)
9. K. Salama, V. Selymanickam, L. Gao, K. Sun, High-current density in bulk $YBa_2Cu_3O_x$ superconductor. Appl. Phys. Lett. **54**, 2352–2354 (1989)
10. T. Egi, J.G. Wen, K. Kuroda, H. Unoki, N. Koshizuka, High-current density of $Nd(Ba, Nd)_2Cu_3O_{7-x}$ single-crystal. Appl. Phys. Lett. **67**, 2406–2408 (1995)
11. S. Jin, T.H. Tiefel, R.C. Sherwood, M.E. Davis, R.B. Van Dover, G.W. Kammlott, R.A. Fasrnacht, H.D. Keith, High critical currents in Y-Ba-Cu-O superconductors. Appl. Phys. Lett. **52**, 2074–2076 (1988)
12. G. Yildirim, Determination of optimum diffusion annealing temperature for Au surface-layered Bi-2212 ceramics and dependence of transition temperatures on disorders. J. Alloys Compd. **699**, 247–255 (2017)
13. O.O. Oduleye, S.J. Penn, N.M. Alford, The mechanical properties of (Bi-Pb) SrCaCuO Supercond. Sci. Technol **11**, 858–865 (1998)
14. W.F. Smith, *Principles of Materials Science and Engineering* (McGraw-Hill, New York, 2001).
15. E. Bruneel, J. Degrieck, I. Van Driessche, S. Hoste, Mechanical properties of Bi-2223/Ag bulk composites. Physica C **372**, 1063–1066 (2002)

16. E. Haque, M.A. Hossain, Elastic, magnetic, transport and electronic properties of no centrosymmetric M2Mo3N (M = Fe Co, Ni, Rh): a first-principles study. J. Alloys Comp. **748**, 117–126 (2018)
17. K.Y. Choi, I.S. Jo, S.C. Han, Y.H. Han, T.H. Sung, M.H. Jung, G.S. Park, S.I. Lee, High and uniform critical current density for large-size $YBa_2Cu_3O_{7-\delta}$ single crystals. Curr. Appl. Phys. **11**, 1020–1023 (2011)
18. H.H. Xu, L. Cheng, S.B. Yan, D.J. Yu, L.S. Guo, X. Yao, Recycling failed bulk YBCO superconductors using the NdBCO/YBCO/MgO film-seeded top-seeded melt growth method. J. Appl. Phys. **111**, 103910 (2012)
19. O. Ozturk, E. Asikuzun, M. Coskunyurek, N. Soylu, A. Hancerliogullari, A. Varilci, C. Terzioglu, The effect of Nd_2O_3 addition on superconducting and structural properties and activation energy calculation of Bi-2212 superconducting system. J. Mater. Sci: Mater. Electron. **25**, 444–453 (2014)
20. R.P. Aloysius, P. Guruswamy, U. Syamaprasad, Enhanced flux pinning in (Bi, Pb)-2223 superconductor by Nd addition. Supercond. Sci. Technol. **18**, 427–431 (2005)
21. M. Abbas, A. Abdulridh, A. Jassim, F. Hashim, Physical properties of nanoparticles Nd added $Bi_{1.7}Pb_{0.3}Sr_2Ca_2Cu_3O_y$ superconductors. AIP Conf. Proc. **1968**, 030009 (2018)
22. K. Kumari, R.K. Singhal, K.B. Garg, M. Heinonen, J. Leiro, A. Gupta, S.K. Agarwal, Photoemission study of Ba^{2+} and Nd^{3+} substitution for Ca^{2+} in the BSCCO (2212) superconducting system. Indian J. Phys. **77A**, 333–339 (2003)
23. O. Ozturk, E. Asikuzun, S. Kaya, G. Yildirim, M.B. Turkoz, A. Kilic, Improvement of the nature of indentation size effect of Bi-2212 superconducting matrix by doped Nd inclusion and theoretical modeling of new matrix. J. Supercond. Nov. Magn. **27**, 1403–1412 (2014)
24. H. Bagiah, S.A. Halim, S.K. Chen, K.P. Lim, M.M. Awang Kechik, Effects of Rare Earth Nanoparticles (M = Sm_2O_3, -Ho_2O_3, Nd_2O_3) addition on the microstructure and superconducting transition of $Bi_{1.6}Pb_{0.4}Sr_2Ca_2Cu_3O_{10+\delta}$. Ceram. Sains Malays. **45**, 643–651 (2016)
25. R.P. Aloysius, P. Guruswamy, U. Syamaprasad, Enhanced critical current density in (Bi, Pb)-2223 superconductor by Nd addition in low percentages. Physica C **426**, 556–562 (2005)
26. B. Ozkurt, A. Ekicibil, M.A. Aksan, B. Ozcelik, M.E. Yakıncı, K. Kiymac, Structural and Physical Properties of Nd Substituted Bismuth Cuprates $Bi_{1.7}Pb_{0.3-x}Nd_xSr_2Ca_3Cu_{4-}O_{12+y}$. J. Low Temp. Phys. **149**, 105–118 (2007)
27. R. Awad, A.I. Abou-Aly, M.M.H. Abdel Gawad, I.G. Eldeen, The influence of SnO_2 nano-particles addition on the Vickers microhardness of (Bi, Pb)-2223 superconducting phase. J. Supercond. Nov. Magn. **25**, 739–745 (2012)
28. N.K. Saritekin, M. Pakdil, G. Yildirim, M. Oz, T. Turgay, Decrement in metastability with Zr nanoparticles inserted in Bi-2223 superconducting system and working principle of hybridization mechanism. J. Mater. Sci: Mater. Electron. **27**, 956–965 (2016)
29. S. Martin, M. Gurvitch, C.E. Rice, A.F. Hebard, P.L. Gammel, R.M. Fleming, A.T. Fiory, Nonlinear temperature-dependence of the normal-state resistivity in $YBa_2Cu_4O_{8\delta-y}$ films. Phys. Rev. B **39**, 9611–9613 (1989)
30. D.M. Newns, P.C. Pattnaik, C.C. Tsuei, Role of vanhove singularity in high temperature superconductors-mean field. Phys. Rev. B **43**, 3075–3084 (1991)
31. G. Yildirim, Beginning point of metal to insulator transition for Bi-2223 superconducting matrix doped with Eu nanoparticles. J. Alloys Compd. **578**, 526–535 (2013)
32. A.E. Koshelev, P. LeDoussal, V.M. Vinokur, Columnar defects and vortex fluctuations in layered superconductors. Phys. Rev. Condens. Matter. B **53**, R8855–R8858 (1996)
33. A.A. Abrikosov, L.P. Gor'kov, Contribution to the theory of superconducting alloys with paramagnetic impurities. Zh. Eksp. Teor. Fiz **39**(1960), 1781–1796 (1960)
34. M.B. Turkoz, S. Nezir, A. Varilci, G. Yildirim, M. Akdogan, C. Terzioglu, Experimental and theoretical approaches on magnetoresistivity of Lu-doped Y-123 superconducting ceramics. J. Mater. Sci. Mater. Electron **24**, 1536–1545 (2013)
35. M.D. Sumption, M. Bhatia, S.X. Dou, M. Rindfliesch, M. Tomsic, L. Arda, M. Ozdemir, Y. Hascicek, E.W. Collings, Irreversibility field and flux pinning in MgB_2 with and without SiC additions. Supercond. Sci. Technol. **17**, 1180–1184 (2004)
36. M.S. Ososfky, R.J. Soulen, S.A. Wolf, J.M. Broto, J.M. Rakoto, J.C. Ousset, G. Coffe, S. Askenazy, P. Pari, I. Bozovic, J.N. Eckstein, G.F. Virshup, Anomalous temperature dependence of the upper critical magnetic field in Bi-Sr-Cu-O. Phys. Rev. Lett. **71**, 2315–2318 (1993)
37. H. Kitaguchi, A. Matsumoto, H. Hatakeyama, H. Kumakura, High temperature performance of MgB_2 powder-in-tube composite tapes. Supercond. Sci. Technol. **17**, S486–S489 (2004)
38. M. Dogruer, G. Yildirim, C. Terzioglu, Effect of annealing temperature on magnetoresistivity, activation energy, irreversibility and upper critical field of the Cu-diffused MgB_2 bulk superconductors. J. Mater. Sci. Mater. Electron. **24**, 392–401 (2013)
39. X.J. Chen, V.V. Struzhkin, Z.G. Wu, H.Q. Lin, R.J. Hemley, H.K. Mao, Unified picture of the oxygen isotope effect in cuprate superconductors. Proc. Natl. Acad. Sci. USA **104**, 3732–3735 (2007)
40. M. Dogruer, C. Terzioglu, G. Yildirim, M. Pakdil, Y. Zalaoglu, Decrement of crack propagation in bulk Bi-2223

superconducting ceramics with Sn-diffusion annealing temperature. J Mater Sci: Mater Electron **26**, 6013–6019 (2015)
41. M. Dogruer, C. Terzioglu, G. Yildirim, O. Gorura, Significant change in mechanical properties of $YBa_2Cu_3O_{7-x}$bulk superconductors diffused with Sn nanoparticles. J. Supercond. Nov. Magn. **27**, 755–761 (2014)
42. M. Dogruer, F. Karaboga, G. Yildirim, C. Terzioglu, Comparative study on indentation size effect, indentation cracks and superconducting properties of undoped and MgB_2 doped Bi-2223 ceramics. J. Mater. Sci: Mater. Electron. **24**, 2327–2338 (2013)
43. O. Ozturk, M. Erdem, E. Asikuzun, O. Yildiz, G. Yildirim, A. Varilci, C. Terzioglu, Investigation of indentation size effect (ISE) and micro-mechanical properties of Lu added $Bi_2Sr_2CaCu_2O_y$ ceramic superconductors. J. Mater. Sci: Mater. Electron. **24**, 230–238 (2013)
44. W. Abdeen, S. Marahba, R. Awad, A.I. Abou Aly, I.H. Ibrahim, M. Matar, Electrical and mechanical properties of (Bi, Pb) -2223 substituted by holmium. J. Adv. Ceram. **5**, 54–69 (2016)
45. O. Uzun, U. Kolemen, S. Çelebi, N. Guclu, Modulus and hardness evaluation of polycrystalline superconductors by dynamic microindentation technique. J. Eur. Ceram. Soc. **25**, 969–977 (2005)
46. A. Toplu, I. Karaca, U. Kolemen, Calculation of true hardness value of Zn added (BiPb)SrCaCuO superconductor by different models. Ceram. Int. **41**, 953–960 (2015)
47. O. Sahin, O. Uzun, M.S. Lizer, H. Gocmez, U. Kolemen, Dynamic hardness and elastic modulus calculation of porous SiAlON ceramics using depth-sensing indentation technique. J. Eur. Ceram. Soc. **28**, 1235–1242 (2008)
48. I. Karaca, O. Uzun, U. Kolemen, F. Yılmaz, O. Sahin, Effects of ZnO addition on mechanical properties of $Bi_{1.84}Pb_{0.34}Sr_{1.91}Ca_{2.03}Cu_{3.06}O_{10}$ prepared by a wet technique. J. Alloys Compd. **476**, 486–491 (2009)
49. S. Kaya, D. Akcan, O. Ozturk, L. Arda, Enhanced mechanical properties of yttrium doped ZnO nanoparticles as determined by instrumented indentation technique. Ceram. Int. **44**, 10306–10314 (2018)
50. R. Terzioglu, The structural and mechanical properties of Gd and Nd substituted double layered $LaCaMnO_7$ ceramics. J. Alloys Compd. **797**, 1173–1180 (2019)